Journal of Magnetic Resonance 303 (2019) 105–114

Contents lists available at ScienceDirect

Journal of Magnetic Resonance

journal homepage: www.elsevier.com/locate/jmr

Binding of tetracycline to its aptamer determined by 2D-correlated Mn^{2+} hyperfine spectroscopy

Thilo Hetzke [a], Alice M. Bowen [b], Marc Vogel [c], Maximilian Gauger [a], Beatrix Suess [c], Thomas F. Prisner [a,*]

[a] Institute of Physical and Theoretical Chemistry and Center of Biomolecular Magnetic Resonance, Goethe University Frankfurt, Frankfurt am Main, Germany
[b] Center for Advanced Electron Spin Resonance (CAESR), Inorganic Chemistry Laboratory, Department of Chemistry, University of Oxford, Oxford, United Kingdom
[c] Department of Biology, Technical University of Darmstadt, Darmstadt, Germany

ARTICLE INFO

Article history:
Received 13 March 2019
Revised 16 April 2019
Accepted 17 April 2019
Available online 28 April 2019

Keywords:
Tetracycline aptamer
Metal binding
Mn^{2+} ions
Hyperfine spectroscopy
2D ELDOR-detected NMR
THYCOS

ABSTRACT

The tetracycline-binding RNA aptamer (TC-aptamer) binds its cognate ligand the antibiotic tetracycline (TC) via a Mg^{2+} or Mn^{2+} ion with high affinity at high divalent metal ion concentrations ($K_D = 800$ pM, $\geqslant$10 mM). These concentrations lie above the physiological divalent metal ion concentration of ca. 1 mM and it is known from literature, that the binding affinity decreases upon decreasing the divalent metal ion concentration. This work uses a Mn^{2+} concentration of 1 mM and 1D-hyperfine experiments reveal two pronounced ^{31}P couplings from the RNA besides the ^{13}C signal of ^{13}C-labeled TC. From these 1D-hyperfine data alone, however, no conclusions can be drawn on the binding of TC. Either TC may bind via Mn^{2+} to the aptamer or TC may form a free Mn-TC complex and some Mn^{2+} also binds to the aptamer. In this work, we show using 2D-correlated hyperfine spectroscopy at Q-band frequencies (34 GHz), that the ^{13}C and ^{31}P signals can be correlated; thus arising from a single species. We use THYCOS (triple hyperfine correlation spectroscopy) and 2D ELDOR-detected NMR (2D electron electron double resonance detected NMR) for this purpose showing that they are suitable techniques to correlate two different nuclear spin species (^{13}C and ^{31}P) on two different molecules (RNA and TC) to the same electron spin (Mn^{2+}). Out of the two observed ^{31}P-hyperfine couplings, only one shows a clear correlation to ^{13}C. Although THYCOS and 2D EDNMR yield identical results, 2D EDNMR is far more sensitive. THYCOS spectra needed a time factor of $\times$20 in comparison to 2D EDNMR to achieve a comparable signal-to-noise.

1. Introduction

RNA aptamers describe a class of typically short RNA molecules, that bind a specific small molecule with high affinity and that have potential applications in diagnostic and therapeutic medicine [1]. The tetracycline-binding RNA aptamer (TC-aptamer) was identified by SELEX (systematic evolution of ligands by exponential enrichment) by Berens et al. [2]. It is known from the crystal structure [3], that the aptamer binds its cognate ligand tetracycline (TC) via a Mg^{2+} ion. The crystal structure reveals several additional Mg^{2+} ions that are bound by the TC-aptamer. The TC-aptamer is characterized by a very high affinity toward its ligand ($K_D = 800$ pM at 10 mM Mg^{2+}) [4]. In addition, the TC-aptamer is one of only a few aptamers that are known to function *in vivo*, where it can control translation and splicing [5–7]. These aspects, paired with the non toxicity and good cell permeability of the ligand [8], make the TC-aptamer a promising artificial riboswitch.

Recent spectroscopic (fluorescence spectroscopy, time-correlated single photon counting spectroscopy and pulsed dipolar electron paramagnetic resonance (EPR) spectroscopy) and thermodynamic studies (isothermal titration calorimetry (ITC), melting curve analysis and circular dichroism spectroscopy) focused on investigating the folding kinetics, the global structure and the conformational flexibility in the presence and absence of TC and its dependence on Mg^{2+} [9–12]. In contrast to the aforementioned studies, this work directly studies the binding of the divalent metal ion in the ligand binding pocket using pulsed EPR hyperfine spectroscopy. This is achieved by replacing diamagnetic Mg^{2+} with paramagnetic Mn^{2+}, which is common practice [13–15], as Mg^{2+} and Mn^{2+} share similar coordination chemistry properties. ITC measurements of the aptamer with Mn^{2+} instead of Mg^{2+} yielded identical binding affinities (Fig. S1) at high divalent metal ion concentrations.

Fig. 1A shows the ligand binding pocket of the TC-aptamer based on the crystal structure [3]. As can be seen, TC coordinates via its *O*11 and *O*12 oxygens (Fig. 1B) to the divalent metal ion. The divalent metal ion is further stabilized by a *pro-*R_P oxygen of

* Corresponding author.
E-mail address: prisner@epr.uni-frankfurt.de (T.F. Prisner).

https://doi.org/10.1016/j.jmr.2019.04.011
1090-7807/

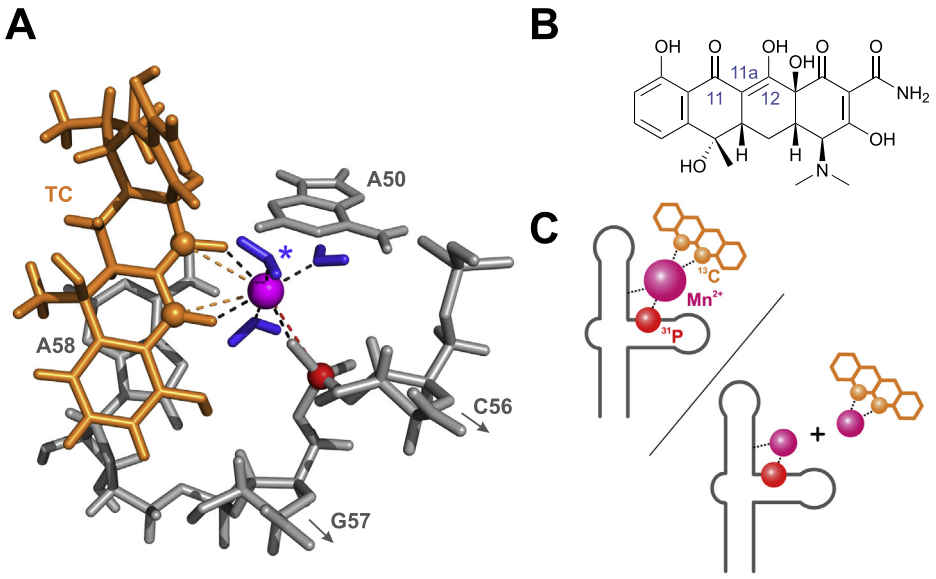

Fig. 1. (A) Ligand binding pocket of the TC-aptamer based on the crystal structure by Xiao et al. [3]. The ligand TC is shown in orange and the nucleobases, which form the binding pocket, are shown in grey (*A50*, *C56*, *G57* and *A58*). Mn^{2+} ions and water molecules are depicted in magenta and blue, respectively. The water molecule marked with an asterisk was not resolved in the crystal structure. (B) Chemical structure of the antibiotic TC. (C) Possible binding models of Mn^{2+} to the aptamer and TC. Depending on the K_D values, TC-binding might be different at an equimolar RNA/Mn^{2+}/TC concentration ratio: TC might interact with the RNA via a Mn^{2+} chelate complex (upper left) or TC might form a separate Mn-TC complex, while remaining Mn^{2+} ions still interact with the RNA (lower right). (For interpretation of the references to colour in this figure legend, the reader is referred to the web version of this article.)

the phosphate backbone of nucleobase *G*57. The crystal structure distance of the *O*11- and *O*12-adjacent carbon atoms to the divalent metal ion is 0.31 nm in both cases, whereas the crystal structure distance of the phosphorous atom to the divalent metal ion is 3.3 nm. Under the assumption that the point-dipole approximation applies, the axial (or dipolar) component T of the hyperfine tensor $\boldsymbol{A}$ is inversely proportional to r^3:

$$\boldsymbol{A} = a_{iso}\boldsymbol{1} + T\begin{pmatrix} -1 & 0 & 0 \\ 0 & -1 & 0 \\ 0 & 0 & 2 \end{pmatrix}, \tag{1a}$$

$$T = \frac{\mu_0}{4\pi h}\frac{g_e\beta_e g_n\beta_n}{r^3}. \tag{1b}$$

a_{iso} and T in Eq. (1a) describe the isotropic and axial component of the hyperfine tensor $\boldsymbol{A}$. Eq. (1b) then yields dipolar hyperfine couplings of $T_{13C} = 0.65$ MHz and $T_{31P} = 1.08$ MHz. Both carbon and phosphorous distances found in the crystal structure are very similar to previously published ^{13}C-Mn^{2+} and ^{31}P-Mn^{2+} hyperfine studies [16–19] and should therefore be readily observable with pulsed hyperfine EPR spectroscopy.

A frequently encountered problem in biochemistry is whether two different molecules *A* and *B* interact at the same time with molecule *C* or not. Examples include nucleic acid aptamers that bind via metal ions to its cognate ligand [3], metal ions that mediate the formation of protein-RNA complexes [20] or membrane proteins that interact via metal ions with an adenosine triphosphate [21]. In case of the TC-aptamer, the binding of TC via a divalent metal ion to the RNA is known to decrease at low Mg^{2+} concentrations [11]. In addition, the free Mn-TC complex [22,23] can potentially interfere with formation of a ternary RNA-Mn-TC complex (Fig. 1C). In this work, it is shown that pulsed 2D-hyperfine spectroscopy is a suitable technique to confirm formation of a ternary RNA-Mn-TC complex at equimolar RNA/Mn^{2+}/TC concentration ratios. Although similar findings can also be obtained by ITC experiments and fluorescence spectroscopy [11], 2D-hyperfine spectroscopy offers the advantage of looking at the ternary complex on an atomistic level. Consequently, 2D-hyperfine data provide a more detailed description of the investigated ternary complex, *e.g.*, which nuclei and which hyperfine coupling are incorporated in the center of the ternary complex.

2. Population-transfer 2D-correlated hyperfine spectroscopy

Pulsed hyperfine EPR spectroscopy describes a wide array of techniques that probe the hyperfine interaction of coupled electron and nuclear spins. Hyperfine spectroscopy methods such as ENDOR (electron nuclear double resonance) and ESEEM (electron spin echo envelope modulation) are often used to study paramagnetic transition metals in nucleic acids and proteins, with the goal of elucidating the local geometry of the paramagnetic cofactor [24–27,18,28,29]. Since the 2000s, the ELDOR-detected NMR technique (electron electron double resonance detected NMR, EDNMR) [30] has gained interest as a method for measuring hyperfine or even quadrupole interactions of nitroxides and paramagnetic transitions metals. Although primarily performed at W-band frequencies (94 GHz) [31–35] to increase the spectral resolution of different nuclear species and to decrease the spectral overlap of the central blindspot and resonances of low-γ nuclei, EDNMR was recently shown to be applicable at Q-band frequencies (34 GHz) as well [36,37].

One of the first pulsed 2D-hyperfine spectroscopy techniques was the TRIPLE experiment [40], in which a Davies ENDOR sequence was expanded by a second RF pulse. Another 2D-hyperfine population transfer technique is the THYCOS (triple hyperfine correlation spectroscopy) experiment [38,41,42], in which the first RF pulse gets replaced by a typically long and weakly powered ELDOR pulse (Fig. 2A). Finally, both RF pulses can be replaced by two ELDOR pulses, resulting in a 2D EDNMR experiment [39,43,42] (Fig. 2B).

THYCOS and 2D EDNMR spectra can be understood by picturing an energy ladder diagram of a 3-spin system, consisting of an electron spin with $S = 1/2$ and two nuclear spins with $I_1 = 1/2$ and $I_2 = 1/2$. If one assumes a positive nuclear g-value (*e.g.*, ^{13}C, ^{31}P, ^{1}H), a positive isotropic hyperfine coupling a_{iso} and the

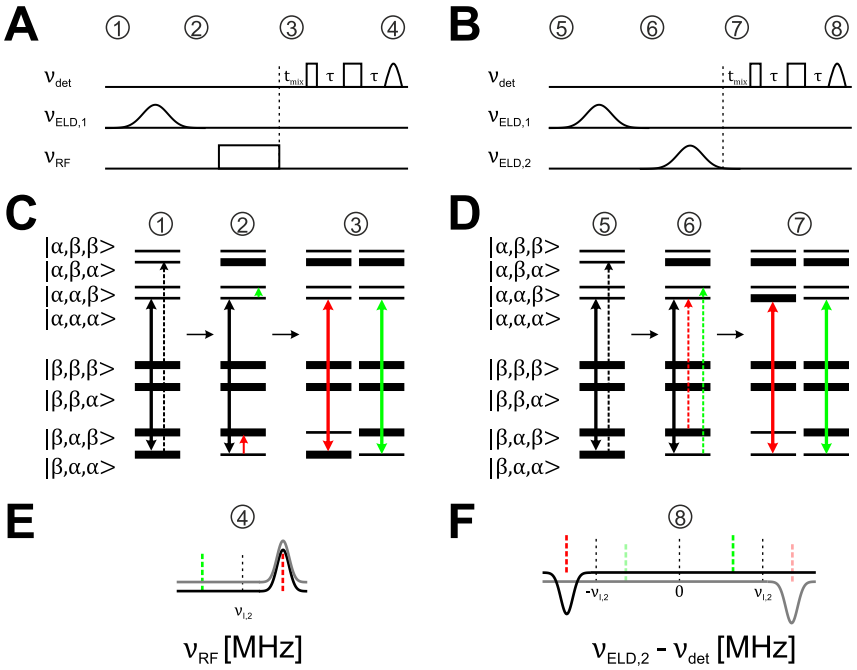

Fig. 2. (A and B) Pulse sequence of a THYCOS [38] (left) and a 2D EDNMR [39] (right) experiment. Gaussian-shaped ELDOR pulses were used to minimize the spectral overlap of detection and ELDOR pulses. (C and D) Energy ladder diagrams for a weakly coupled 8-level system, consisting of an electron spin with $S = 1/2$ and two different nuclear spins with $I_1 = 1/2$ and $I_2 = 1/2$ ($g_N, a_{iso} > 0$). Bold black arrows depict the detected allowed EPR transition, whereas the dashed black arrows (① & ⑤) depict the first ELDOR pulse, which is on-resonance with a forbidden transition of nuclei I_1. ②: For THYCOS, two allowed NMR transitions of nuclei I_2 (solid green and red arrows) are associated with the detected EPR transition. ⑥: For 2D EDNMR, two forbidden transitions of nuclei I_2 (dashed green and red arrows) are associated with the detected EPR transition. ③ & ⑦: Spin population before the echo detection sequence in THYCOS and 2D EDNMR respectively for excitation of the two nuclear transitions. (E and F) Depending on which transitions are excited, positive signals (THYCOS, dashed red line), no signals at all (2D EDNMR and THYCOS, dashed green lines) or negative signals (2D EDNMR, dashed red line) are expected. Pale dashed lines correspond to 2D EDNMR signals that stem from excitation of another allowed EPR transition ($|\beta,\alpha,\beta\rangle \leftrightarrow |\alpha,\alpha,\beta\rangle$, grey model spectra). (For interpretation of the references to colour in this figure legend, the reader is referred to the web version of this article.)

weak-coupling regime ($\nu_I > a_{iso}/2$), an energy ordering of spin levels as shown in Fig. 2C and D is expected. If ν_{det} is set to monitor the intensity of the allowed EPR transition $|\beta,\alpha,\alpha\rangle \leftrightarrow |\alpha,\alpha,\alpha\rangle$ (bold black arrows in Fig. 2C and D), only one forbidden transition ($\Delta m_S = \pm 1, \Delta m_I = \pm 1$) for nuclei I_1 exists, that has a larger resonance frequency than ν_{det} ($|\beta,\alpha,\alpha\rangle \leftrightarrow |\alpha,\beta,\alpha\rangle$, dashed black arrow in Fig. 2C and D). If one assumes that the ELDOR pulse inverts the population of the forbidden transitions of the 3-spin model system, excitation of the aforementioned forbidden transition of nucleus I_1 would lead to zero echo intensity in the detection channel.

For THYCOS, next a RF pulse is applied, the frequency of which is varied to sample the allowed NMR transitions that are associated with nucleus I_2 (green and red arrows in Fig. 2C, ②). The detected echo intensity stays at zero if transition $|\alpha,\alpha,\alpha\rangle \leftrightarrow |\alpha,\alpha,\beta\rangle$ gets excited and becomes positive if transition $|\beta,\alpha,\alpha\rangle \leftrightarrow |\beta,\alpha,\beta\rangle$ gets excited (bold green and red arrows in Fig. 2C, ③).

For 2D EDNMR, a second variable frequency ELDOR pulse is applied to probe the forbidden transitions of nucleus I_2 (dashed green and red arrows in Fig. 2D, ⑥). If the ELDOR pulse induces the transition $|\beta,\alpha,\alpha\rangle \leftrightarrow |\alpha,\alpha,\beta\rangle$ the detected echo intensity remains zero. However, the intensity becomes negative if transition $|\beta,\alpha,\beta\rangle \leftrightarrow |\alpha,\alpha,\alpha\rangle$ gets excited (bold green and red arrows in Fig. 2D, ⑦). It should be noted that in reality, long ELDOR pulses act as saturation pulses on the forbidden transitions, which may lead to slightly different signal intensities due to polarization transfer processes during the ELDOR pulse.

The expected THYCOS and 2D EDNMR model spectra are shown in Fig. 2E and F. Due to the inhomogeneous EPR linewidth, spin packets of different allowed EPR transitions have a significant spectral overlap. For this reason, the detection pulses will excite several allowed EPR transitions of the 3-spin model system simultaneously. As a consequence, the THYCOS and 2D EDNMR slices observed experimentally are a superposition of the slices of all the excited allowed EPR transitions.

Until now it has been assumed that one forbidden transition (out of two) of nucleus I_1 is excited selectively by the first ELDOR pulse (① and ⑤ in Fig. 2C and D). This is, for example, the case for the ^{31}P couplings presented in this work. If, however, the coupling is small and hence the splitting of the signals around the Larmor frequency of nucleus I_1 is small, both forbidden transitions can be excited at the same time. In such a case, more THYCOS and 2D EDNMR signals will appear (positive in THYCOS and negative in 2D EDNMR) at frequencies marked with green dashes in Fig. 2E and F.

Additionally, THYCOS and 2D EDNMR spectra will look slightly different, if the RF pulse or the second ELDOR pulse excites transitions associated with the nucleus that was excited by the first ELDOR pulse (see Fig. S2 for an explanation).

W-band THYCOS was previously used to separate different ^{1}H resonances and to determine the sign of the hyperfine coupling in a Cu(II)-L-histidine complex [38] and to assign ^{14}N resonances via ^{1}H-^{14}N THYCOS to the type 1 Cu(II) site in ascorbate oxidase (out of one type 1 Cu(II) site and one type 2 Cu(II) site) [41]. W-band 2D EDNMR and quantum chemical calculations were used to elucidate the ^{33}S-hyperfine tensor of type 1 Cu(II)-azurin, which proved difficult with a congested ^{14}N-^{33}S 1D EDNMR spectrum alone [43]. Recently, W-band $^{14/15}$N-^{31}P THYCOS was used to resolve the coordination geometry of Mn-ATP in frozen solution [42]. In this work, it is shown that ^{13}C and ^{31}P nuclei, incorporated in two different molecules (TC and RNA), can be used to correlate hyperfine signals to the same electron spin associated with a single Mn^{2+} ion.

3. Material and methods

3.1. Sample preparation

In vitro transcription was identical to a procedure published previously [11]. Before EPR measurements, the RNA was dialyzed with a buffer (100 mM triethanolamine (TEA) pH 7.5, 1 M KCl) to replace remaining Na^+ ions from the RNA purification process with K^+ ions. Amicon filters with a cut-off of 10 kDa and a sample volume of 0.5 ml were used for dialysis. The aqueous RNA solution was diluted with the buffer solution to a volume of 0.5 ml, then the solution was spun at 10,000 rpm until the solution was concentrated to a volume of 50 µl. The RNA was dialyzed four times with the buffer solution and four times with DEPC-treated MilliQ water. At Q-band, the difference between the ^{13}C- and ^{23}Na-Larmor frequency is only 0.7 MHz ($\nu_{13C} = 12.7$ MHz and $\nu_{23Na} = 13.5$ MHz). The Larmor frequency of ^{40}K (93.2% natural abundance) at Q-band frequencies is $\nu_{40K} = 2.3$ MHz. In contrast to ^{23}Na, ^{40}K should therefore not interfere with any ^{13}C or ^{31}P resonances. 1D EDNMR spectra before and after dialysis of Na^+ with K^+ are shown in the supporting information (Fig. S3). For each experiment, aliquots of the dialyzed RNA were lyophilized and dissolved in a buffer containing 2mM $Mn(ClO_4)_2$, 100 mM TEA and 1 M KCl at pH = 7.5. Depending on the sample, the buffer either contained 2 mM TC, 2 mM ^{13}C-labeled TC (Romer Labs Diagnostic) or no TC at all. 50% glycerol (v/v) was added as a glassing agent. The final RNA concentration was 1 mM. All chemicals were certified RNase free. 10 µl of the buffered RNA solutions were then transferred into 1.6 mm (outer diameter) Suprasil tubes. Samples were shock-frozen in liquid nitrogen *prior* to being inserted into the resonator.

3.2. Pulsed EPR measurements

Pulsed EPR hyperfine experiments at Q-band frequencies (33.77 GHz) were performed on a Bruker Elexsys E580 spectrometer equipped with a dielectric EN 5170 DE ENDOR probehead. The temperature was kept at 5 K using a continuous-flow helium cryostat (CF935) and an ITC 502 temperature control unit, both from Oxford Instruments. A 150 W traveling-wave tube amplifier by Applied Systems Engineering was used for microwave amplification. Pulses were created by a Bruker-manufactured arbitrary waveform generator (SpinJet AWG). For ENDOR measurements, RF frequencies were generated out of a DICE-II box and amplified by an externally blanked RF amplifier by Dressler (2 kW, LPPA 10020 LF). A low-pass filter (RF limited DF-3000) with a cutoff frequency of 30 MHz and a Bruker-supplied noise suppressor where used to avoid 3rd and 5th order ^1H harmonics and to enhance signal quality.

For ^{31}P-Davies ENDOR, the sequence $2t_p - t_{RF} - t_{mix} - t_p - \tau - 2t_p - \tau - echo$ with $t_p = 100$ ns and $\tau = 1$ µs was used. The length of the RF pulse was optimized with nutation experiments which resulted in $t_{RF} = 25$ µs for ^{31}P. The frequency of the RF pulse was varied ±9 MHz around the ^{31}P-Larmor frequency ($\nu_{31P} = 20.7$ MHz) with an increment of 50 kHz (361 points). The integration width of the echo was set to 800 ns, centered around the echo maximum. For ^{13}C-Mims ENDOR, the sequence $t_p - \tau - t_p - t_{RF} - t_{mix} - t_p - \tau - echo$ with $t_p = 10$ ns and $\tau = 320$ ns was used. The RF pulse was optimized near the ^{13}C-Larmor frequency to a length of $t_{RF} = 27.5$ µs. The echo integration width was set to 36 ns, centered around the echo maximum. The sweep width of the RF pulse was 8 MHz, centered around the ^{13}C-Larmor frequency ($\nu_{31P} = 12.7$ MHz), with a frequency increment of 25 kHz (321 points).

1D and 2D EDNMR spectra were acquired using a $(t_{ELD} - t-)t_{ELD} - t_{mix} - t_p - \tau - 2t_p - \tau - echo$ sequence, with $\tau = 1$ µs, $t_{mix} = 9$ µs and $t_p = 400$ ns. For 1D EDNMR experimemts an ELDOR pulse length of $t_{ELD} = 9$ µs was used, for 2D EDNMR experiments an ELDOR pulse length of $t_{ELD} = 40$ µs was used. For 2D EDNMR experiments, longer ELDOR pulses yielded more intense correlation signals at the cost of a slight spectral broadening. The integration width of the echo was 1400 ns for all EDNMR experiments, centered around the echo maximum. For 1D EDNMR experiments, an ELDOR sweep width of 440 MHz, starting at −220 MHz and with a frequency increment of 300 kHz, was used. For 2D EDNMR experiments where the frequency of both ELDOR pulses was varied (complete 2D EDNMR spectra), the ELDOR sweep width was decreased to 80 MHz, starting at −40 MHz and with a frequency increment of 300 kHz. For 2D EDNMR slices, where only the frequency of first ELDOR pulse was varied and the frequency of the second ELDOR pulse was kept constant, the x-axis resolution was increased to 200 kHz with an ELDOR sweep width of 54 MHz (centered symmetrically around the spectrometer frequency). A higher resolution, while maintaining a sweep width of 54 MHz, was not possible due to a limited AWG pulse sequence memory space. All EDNMR experiments utilized a shot repetition time of 3 ms, 50 shots per point and Gaussian shaped ELDOR pulses to decrease the spectral overlap with detection pulses [44,30]. All EDNMR experiments (1D and 2D) used an ELDOR amplitude of $\omega_{ELD} = 1.5 \times 10^7$ rad/s at zero frequency to allow for a comparison of EDNMR intensities of different samples. Moreover, different samples were tuned at the same spectrometer frequency in such a way, that the tuning dip looked as similar as possible.

For THYCOS experiments, the Davies ENDOR sequence was used, with the only difference being a replacement of the first inversion pulse by a 9 µs long Gaussian ELDOR pulse operating at a fixed frequency offset $\Delta\nu$. The amplitude ω_{ELD} was the same as for EDNMR experiments. The RF sweep width and x-axis resolution was identical to Davies ENDOR experiments. ENDOR and THYCOS experiments employed a shot repetition time of 50 ms and 1 shot per point. The random acquisition mode was used to avoid baseline distortions due to heating effects [45].

The ENDOR/1D EDNMR intensity was calculated to $\varepsilon(\nu_{RF/ELD}) = \frac{I_{RF/ELD\ on} - I_{RF/ELD\ off}}{I_{RF/ELD\ off}}$, where $I_{RF/ELD\ off}$ is an averaged signal range with off-resonance ELDOR or RF pulses respectively. A rolling baseline in Mims ENDOR spectra was removed by subtracting a Mims ENDOR spectrum of an unlabeled TC sample from the Mims ENDOR spectrum of the ^{13}C-labeled TC sample and multiplying the result with −1 (Fig. S8). The baseline of Davies ENDOR spectra was corrected by fitting a polynomial to the off-resonance regions of Davies ENDOR spectra. 2D EDNMR spectra were processed as described earlier [39]. 2D EDNMR slices were background-corrected by normalizing a specific slice (*e.g.*, $\Delta\nu_2 = \nu_{13C} = 12.7$ MHz) to the off-resonance intensity of a slice with an off-resonance second ELDOR pulse (*e.g.*, $\Delta\nu_2 = 40.0$ MHz). Subtraction of these two slices then yielded a background-corrected 2D EDNMR slice [42].

t_{mix} describes the time delay between mixing period and detection period. It is increased for variable-mixing-time (VMT) ENDOR experiments (Fig. S11), and kept as short as possible for ENDOR, EDNMR and THYCOS measurements. For ENDOR and THYCOS measurements, t_{mix} is chosen so that the trailing edge of the RF pulse does not interfere with the detection sequence. For EDNMR measurements, t_{mix} is chosen to allow for a decay of electron coherence, which can be created by the ELDOR pulse.

All experiments were performed on the "third" ^{55}Mn-hyperfine transition from the left of the "central" electron transition ($|m_S = -1/2, m_I = -1/2\rangle \leftrightarrow |+1/2, -1/2\rangle$).

4. Results and discussion

4.1. 1D EDNMR

Fig. 3 shows the ^{13}C and ^{31}P region of Q-band EDNMR spectra of different TC-aptamer samples (Fig. S4 contains full-range EDNMR spectra). In the absence of any TC (Fig. 3, blue spectrum), two pronounced ^{31}P-hyperfine couplings with $A_{31P}(1) = 4.8$ MHz and $A_{31P}(2) = 9.3$ MHz are visible. The small signal at the ^{13}C-Larmor frequency ($\nu_{13C} = 12.7$ MHz) is attributed to natural abundance ^{13}C, which is reasonable, as a rather carbon-rich environment is expected for RNA-coordinated Mn^{2+} ions.

The signal at 9 MHz is assigned to the high-frequency component of a hyperfine-split ^{14}N double quantum transition ($\Delta m_S = \pm 1, \Delta m_I = \pm 2$, $2\nu_{14N} = 7.4$ MHz), which is plausible, as Mn^{2+}-coupled ^{14}N nuclei exhibit a rather large quadrupole coupling [46] and therefore have an intrinsically high probability for forbidden transitions. The EDNMR spectrum in the presence of TC (Fig. 3, red spectrum) is essentially identical to the one in the absence of TC. Upon addition of ^{13}C-labeled TC (Fig. 3, green spectrum), the signal around the ^{13}C-Larmor frequency is enhanced. Besides the ^{13}C signal, however, all EDNMR spectra are very similar.

^{31}P couplings are expected for Mn^{2+}-containing RNA systems, as the negatively charged phosphate groups of the RNA backbone coordinate the positively charged Mn^{2+} ion. The difference of 4.5 MHz between the two observed phosphorous couplings is due to different values for the isotropic hyperfine coupling, a_{iso}. For a typical Mn^{2+}-^{31}P first coordination sphere distance of 0.3 nm, a dipolar hyperfine coupling, T, of 1.18 MHz is expected, which cannot explain the splitting of either 4.8 or 9.3 MHz. Interestingly, values similar to $A_{31P}(1)$ and $A_{31P}(2)$ have already been reported in literature for Mn^{2+}-containing RNA systems [25,16,17,28]. A DFT and hyperfine study on Mn^{2+}-phosphate complexes recently also revealed a considerable impact of the pH value on the magnitude of the isotropic hyperfine coupling a_{iso} [47]. Kaminker et al. attributed the larger phosphorous coupling of ≈ 9 MHz to single-stranded RNA (ssRNA) [17]. In our case, we observed an increase in intensity for the outer phosphorous coupling and a decrease in intensity for the inner phosphorous coupling after several freeze-thaw cycles (Fig. S5). The intensity of the carbon signal, originating from ^{13}C-TC, decreased as well. As it is generally known that several freeze-thaw cycles lead to degradation of RNAs and therefore to a higher percentage of shorter ssRNA fragments, these findings are in line with the results of Kaminker et al. [17].

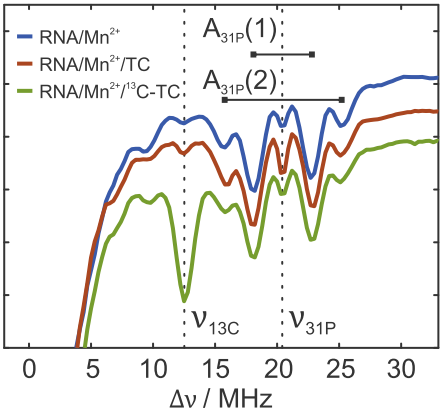

Fig. 3. Q-band 1D EDNMR spectra of different Mn^{2+} complexes. Blue: TC-aptamer with Mn^{2+}, red: TC-aptamer with Mn^{2+} and TC, green: TC-aptamer with Mn^{2+} and ^{13}C-labeled TC. Only the ^{13}C and ^{31}P regions are shown. Larmor frequencies of these nuclei are indicated with dashed lines. Two distinct ^{31}P-hyperfine couplings are visible. (For interpretation of the references to colour in this figure legend, the reader is referred to the web version of this article.)

Full-range EDNMR spectra (Fig. S4) reveal different ^{55}Mn linewidths for the samples presented in Fig. 3. Samples containing unlabelled TC and ^{13}C-labeled TC exhibit a broader ^{55}Mn linewidth than a sample containing RNA and Mn^{2+}. A different lineshape is expected as coordination of TC to Mn^{2+} should lead to a slightly different coordination geometry, e.g., a different hyperfine coupling, a different hyperfine strain and/or a different quadrupole interaction.

Although a clear ^{13}C EDNMR signal is observed (Fig. 3) and subtle differences in the ^{55}Mn EDNMR regions are visible (Fig. S4), it cannot be deduced from these spectra if TC actually coordinates to the RNA at equimolar RNA/Mn^{2+}/TC concentration regimes. For instance, it is known that TC coordinates free Mn^{2+} ions with a dissociation constant of approximately $K_D \approx 100$ μM [22,23], that could compete with the coordination of TC to the RNA.

4.2. ^{31}P-Davies ENDOR and ^{13}C-Mims ENDOR

Fig. 4A shows Q-band ^{31}P-Davies ENDOR spectra of samples whose EDNMR data were already shown in Fig. 3. All Davies ENDOR spectra are essentially identical. Whereas the outer hyperfine coupling $A_{31P}(2)$ displays the expected axial Pake doublet, an interpretation of the isotropic-looking shape of the inner hyperfine coupling $A_{31P}(1)$ is more difficult. It is known that a superposition of hyperfine couplings of different magnitudes leads to a rather isotropic-looking lineshape [47].

A simulation of experimental Davies ENDOR spectra, using the MATLAB toolbox EasySpin [48], required at least four rhombic components for $A_{31P}(1)$ and one axial component for $A_{31P}(2)$ to achieve a good agreement between experimental and simulated data (Fig. S6). The simulation yielded hyperfine coupling constants of $a_{iso}(1) =$ 2.8–4.8 MHz and $T(1) =$ 0.8–0.9 MHz for the inner hyperfine coupling, and coupling constants of $a_{iso}(2) = 9.5$ MHz and $T(2) = 1.1$ MHz for the outer hyperfine coupling (Table S1). Assuming the point-dipole approximation, the dipolar hyperfine couplings translate into ^{31}P-Mn^{2+} distances of $r =$ 0.33–0.34 nm (inner coupling) and $r = 0.31$ nm (outer coupling). Theses distances are in excellent agreement with the extracted ^{31}P-Mn^{2+} distances from the crystal structure [3]. However, the distances cannot be assigned to specific Mn^{2+} binding sites of the TC-aptamer, as the differences of the different crystal structure distances are to small (Figs. S7 and Table S1).

Fig. 4B shows Q-band ^{13}C-Mims ENDOR spectra of a sample containing the TC-aptamer, Mn^{2+} and ^{13}C-labeled TC (green spectrum) and a sample containing just Mn^{2+} and ^{13}C-labeled TC (violet spectrum). The spectrum of the free Mn-TC complex is very similar to the spectrum of the sample containing the TC-aptamer. Both spectra feature two hyperfine couplings: a larger one, whose Pake doublet shape is slightly smeared out by the Mims ENDOR blindspot function (depicted as a dashed grey line in Fig. 4B), and a smaller hyperfine coupling with a splitting of approximately 0.2 MHz. Mims ENDOR spectra with different τ values did not reveal less blindspot-distorted Mims ENDOR spectra (Fig. S9). Simulations of the Mims ENDOR spectra convoluted with a Mims ENDOR blindspot-function are presented in Fig. S9. For the outer hyperfine coupling, two different hyperfine tensors yielded equally good results (possibility one: $a_{iso,1} = 1.3$ MHz, $T_1 = 0.6$ MHz, $r_1 = 0.32$ nm, possibility two: $a_{iso,2} = 0.4$ MHz, $T_2 = 1.2$ MHz, $r_2 = 0.37$ nm). Mims ENDOR experiments with the magnetic field on-resonance with outer electron transitions [49] (Fig. S10), VMT Mims ENDOR experiments [50] (Fig. S11) and DFT-calculations (Figs. S12 and Table S2) favour possibility one ($a_{iso} > T$) over possibility two.

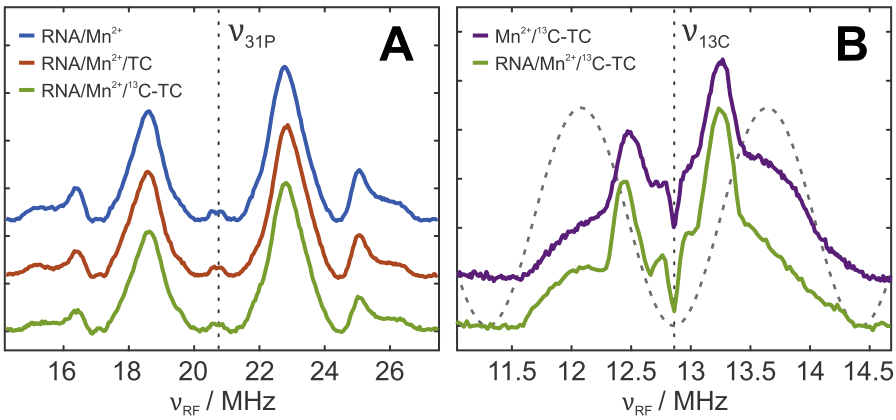

Fig. 4. (A) Q-band ^{31}P-Davies ENDOR spectra of different Mn^{2+} complexes. Blue: TC-aptamer with Mn^{2+}, red: TC-aptamer with Mn^{2+} and TC, green: TC-aptamer with Mn^{2+} and ^{13}C-labeled TC. (B) Q-band ^{13}C-Mims ENDOR spectra of different Mn^{2+} complexes. Purple: Mn^{2+} with ^{13}C-labeled TC, green: TC-aptamer with Mn^{2+} and ^{13}C-labeled TC. A τ value of 330ns was used. The Mims ENDOR blindspot function is shown as a dotted grey line. Larmor frequencies of ^{13}C and ^{31}P are indicated with dashed lines. (For interpretation of the references to colour in this figure legend, the reader is referred to the web version of this article.)

Both spectra in Fig. 4B are proof for binding of TC to Mn^{2+}, however, the binding of TC to the RNA via Mn^{2+} cannot be deduced directly from the Mims ENDOR spectra.

4.3. 2D EDNMR

In order to address the question of the binding of Mn^{2+} to the aptamer and TC we performed Q-band 2D EDNMR measurements on samples with ^{13}C-labeled TC and unlabeled TC. Whereas the labeled sample should feature ^{13}C-^{31}P cross peaks in the case of simultaneous binding of TC to the RNA via Mn^{2+}, no such signals should be present in the unlabeled sample. Fig. 5A shows the minus-plus and plus-plus quadrant of a sample containing RNA, Mn^{2+} and unlabeled TC. The minus-minus and plus-minus quadrant are not shown, as they contain redundant information. Strips to the left and above the 2D EDNMR spectrum show 1D EDNMR spectra with no correlation signals. The plus-plus quadrant is characterized by ^{31}P self-correlations signals on the diagonal. The information content is similar to a 1D EDNMR spectrum, but with a slightly higher spectral resolution.

The signals close to the central blindspot at (5.0,5.0) MHz are assigned to ^{14}N self-correlation signals. We exclude the possibility of these signals being an artifact stemming from an incomplete central blindspot removal by the background correction procedure. In such a case, the signals at (−5.0,5.0) MHz in the minus-plus quadrant should be equally intense.

The minus-plus quadrant of Fig. 5A is characterized by negative cross peaks of the two nuclear spin manifolds of the inner phosphorous coupling at (−22.9,18.1) and (−18.1,22.9) MHz. Negative cross peaks with the phosphorous matrix signal at 20.8 MHz are also visible. No cross peaks of the outer phosphorous couplings could be detected. In contrast to previous work by Kaminker et al. and Ramirez-Cohen et al. [39,43], negative cross peaks are solely confined to the minus-plus quadrant. This behavior was also observed for less complex Mn^{2+} compounds, such as Mn^{2+} with inorganic phosphate (Mn-P_i) and Mn-^{13}C-DOTA (Figs. S16 and S17).

More signals appear at (−5.0,18.1) and (−5.0,22.9) MHz in the minus-plus quadrant and at (5.0,18.1) and (5.0,22.9) MHz in the plus-plus quadrant. Originally these signals were assigned to ^{14}N-^{31}P cross peaks. However, these signals do not show up in the other frequency domain, *e.g.*, (18.1,−5.0) MHz. In addition, one would expect negative cross peaks for heteronuclear 2D EDNMR spectra (Fig. 2F). These cross peaks also have a rather unusual shape, as they point in a "cross-like" manner toward the phosphorous Larmor frequency.

Litvinov et al. attributed similar signals in a recent 2D EDNMR and THYCOS study to off-resonance effects of the ELDOR pulse [42]. In line with these findings we observed similar cross peaks for a sample containing Mn-P_i, which should not contain any ^{14}N resonances. For Mn-^{13}C-DOTA and $[Mn(H_2O)_6]^{2+}$, which contain no ^{31}P resonances, no signals due to off-resonance effects are visible for the frequency range shown in Fig. 5 (Figs. S17 and S18).

The plus-plus quadrant of a sample with ^{13}C-labeled TC (Fig. 5B) is almost identical to the 2D EDNMR spectrum with unlabeled TC, with the only difference being the large ^{13}C self-correlation signal for the labeled sample. The minus-plus quadrant of a ^{13}C-labeled sample is characterized by a positive signal at (−12.7,12.7) MHz. As the ^{13}C-hyperfine coupling is rather small, and the intensities of the different ^{13}C nuclear spin manifolds do severely overlap (Fig. 4B), one only sees a single signal at the ^{13}C-Larmor frequency (instead of two signals as seen for ^{31}P). The most striking differences between Fig. 5A and B are, however, ^{13}C-^{31}P cross peaks at (−18.1,12.7) and (−12.7,18.1) MHz. Cross peaks of ^{13}C and ^{31}P matrix signals are visible at (−20.8,12.7) and (−12.7,20.8) MHz. These cross peaks are a clear sign that TC binds to the TC-aptamer, even at 1 mM Mn^{2+}.

It should be noted, that not all signals (and their intensities) in the 2D EDNMR spectra are completely understood. It is for example unclear why ^{13}C correlation signals of ^{13}C-TC in the minus-plus quadrant are positive (Fig. 5B), whereas the ^{13}C correlation signals of Mn-^{13}C-DOTA in the minus-plus quadrant are negative (Fig. S17). Different cross-relaxation rates and magnitudes of the hyperfine coupling could be an explanation.

Surprisingly, the contour plot in Fig. 5B does not show any cross peaks for the ^{31}P coupling at 22.9 MHz at (−22.9,12.7) and (−12.7,22.9) MHz. In order to get a better insight into ^{13}C-^{31}P cross peaks, we therefore recorded 2D EDNMR slices with an increased resolution and signal-to-noise ratio. Selected 2D EDNMR slices with $\Delta\nu_2$ on-resonance with either the phosphorous nuclear spin manifold at 18.1 MHz or at 22.9 MHz are shown in Fig. 6A and B, respectively. Again, slices for a sample with ^{13}C-labeled TC (green spectra) and unlabeled TC (red spectra) are shown.

The signals at −5.0 and 5.0 MHz in Fig. 6A and B are the "cross-like" signals in Fig. 5A and B due to off-resonance effects of the first ELDOR pulse, while the second ELDOR pulse is exciting a phosphorous transition. It should be noted, that the relative intensities of these signals are reproducible (the signal at −5.0 MHz has a higher intensity than the one at 5.0 MHz if the phosphorous transition at 18.1 MHz is excited and *vice versa*). The reason for this is currently unclear.

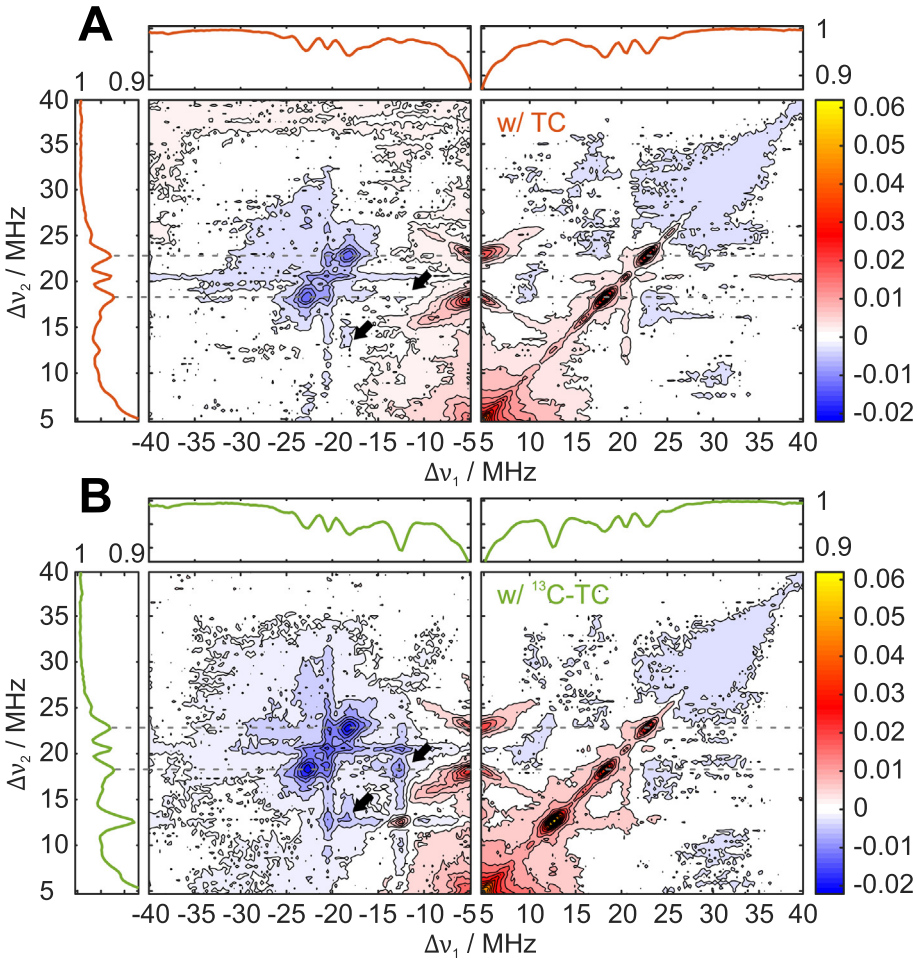

Fig. 5. Background-corrected Q-band 2D EDNMR spectra. (A) TC-aptamer with Mn^{2+} and TC, (B) TC-aptamer with Mn^{2+} and ^{13}C-labeled TC. Only the minus-plus and plus-plus quadrant are shown, as the plus-minus and minus-minus quadrant look identical. Strips to the left and above the 2D EDNMR spectrum show 1D EDNMR spectra that are free of any correlation signals. Black arrows label expected frequency offsets for ^{13}C-^{31}P correlation signals. Dotted grey lines correspond to chosen 2D EDNMR slices that were recorded with a higher resolution and a better signal-to-noise ratio (Fig. 6). Primary 2D EDNMR spectra and all four quadrants of background-corrected 2D EDNMR spectra are presented in the Supporting Information (Figs. S13–S15).

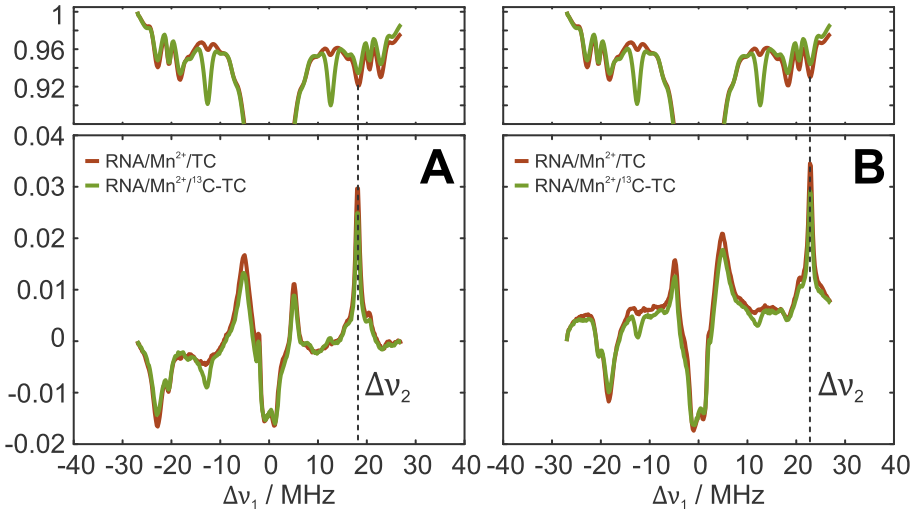

Fig. 6. Individual slices of the Q-band 2D EDNMR spectra shown in Fig. 5 recorded with higher resolution and a better signal-to-noise ratio. (A) 2D EDNMR slices with the frequency of the second ELDOR pulse set to 18.1 MHz. (B) 2D EDNMR slices with the frequency of the second ELDOR pulse set to 22.9 MHz. In both cases, the frequency of the first ELDOR pulse was varied. The slices presented in this figure correspond to horizontal slices in Fig. 5 (marked by dashed lines in Fig. 5). Red: TC-aptamer with Mn^{2+} and TC, green: TC-aptamer with Mn^{2+} and ^{13}C-labeled TC. (For interpretation of the references to colour in this figure legend, the reader is referred to the web version of this article.)

For ^{31}P, the expected signal pattern for a homonuclear 2D EDNMR is observed (Fig. S2), that is, a positive 2D EDNMR signal for the ^{31}P nuclear spin manifold that gets excited by $\Delta\nu_2$ at positive $\Delta\nu_1$ values (*e.g.*, $\Delta\nu_1 = \Delta\nu_2 = 18.1$ MHz), and a negative 2D EDNMR signal for the nuclear transition in the other electron spin manifold at negative $\Delta\nu_1$ values (*e.g.*, $\Delta\nu_1 = -22.9$ MHz).

The ^{13}C-^{31}P cross peak for a labeled sample at −12.7 MHz in Fig. 6A ($\Delta\nu_2 = 18.1$ MHz) was already clearly visible in the 2D EDNMR spectrum in Fig. 5B at (−12.7,18.1) MHz. Fig. 6B shows a clear ^{13}C-^{31}P cross peak for a labeled sample at −12.7 MHz as well ($\Delta\nu_2 = 22.9$ MHz). This cross peak at (−12.7,22.9) MHz was not visible in the complete 2D EDNMR spectrum in Fig. 5B, which is probably due to a combination of an insufficient signal-to-noise ratio and a too small number of contour levels.

Based on 2D EDNMR data alone, it is difficult to make statements about cross peaks involving the outer ^{31}P-hyperfine coupling. The ^{31}P-^{31}P cross peak at negative frequency offsets in Fig. 6B covers an area ranging from approximately −21 to −15.5 MHz. The self-correlation signal of the inner ^{31}P coupling at −18.1 MHz therefore obscures a potential correlation signal of the inner ^{31}P coupling and the outer ^{31}P coupling which should appear at −15.9 MHz.

4.4. THYCOS

To substantiate our 2D EDNMR results, we also performed THYCOS experiments. Although THYCOS is inferior to 2D EDNMR in terms of sensitivity, it offers the advantage that no background correction is needed. If the initial ELDOR pulse is off-resonance to any transition (forbidden or allowed), the RF pulse will have no effect, as the different nuclear spin levels within one electron spin manifold are almost equally populated.

Homonuclear ^{31}P-^{31}P THYCOS yielded the expected peak intensities, that is, a negative THYCOS signal for the ^{31}P nuclear spin manifold that gets excited by the ELDOR pulse, and a positive THYCOS signal for the ^{31}P nuclear spin manifold that is not getting excited by the ELDOR pulse (Fig. S19). A THYCOS effect is observed for the inner as well as for the outer ^{31}P-hyperfine coupling. However, no correlation is observed between these two hyperfine couplings.

For heteronuclear ^{13}C-^{31}P THYCOS, we irradiated the ^{13}C-EDNMR signal with the ELDOR pulse and sampled the ^{31}P region with the RF pulse. The reason for that is that the ^{13}C-EDNMR signal is larger than the ^{31}P-EDNMR signal, which should therefore give a more intense THYCOS signal. Fig. 7 shows THYCOS spectra of samples with unlabeled TC (red spectra) and ^{13}C-labeled TC (green spectra). As expected, no signal is visible for the unlabeled sample, if the ELDOR pulse is on-resonance with the ^{13}C-Larmor frequency (12.7 MHz) or if the ELDOR pulse is off-resonance with any allowed or forbidden transition (35 MHz).

For the ^{13}C-labeled sample, however, clear correlation signals are visible for the inner ^{31}P-hyperfine coupling if the ELDOR pulse is on-resonance with the ^{13}C-Larmor frequency (12.7 MHz). Therefore, the THYCOS spectra confirm the interpretation of the previous 2D EDNMR results. Due to the lower sensitivity of THYCOS, no ^{13}C-^{31}P cross peaks involving the outer ^{31}P-hyperfine coupling could be detected. The relative intensities of the THYCOS signals at 18.1 and 22.9 MHz even match the relative intensities of the 2D EDNMR signals. For both, 2D EDNMR and THYCOS, a smaller ^{13}C-^{31}P correlation signal intensity is observed if the ^{31}P transition at 22.9 MHz is excited (in comparison to the correlation signal involving the ^{31}P transition at 18.1 MHz).

Fig. 2E shows that only a single peak is expected for a heteronuclear THYCOS. As the ^{13}C-hyperfine coupling is, however, rather small, and the intensities of the different nuclear spin manifolds are known to overlap near the ^{13}C-Larmor frequency, the actual

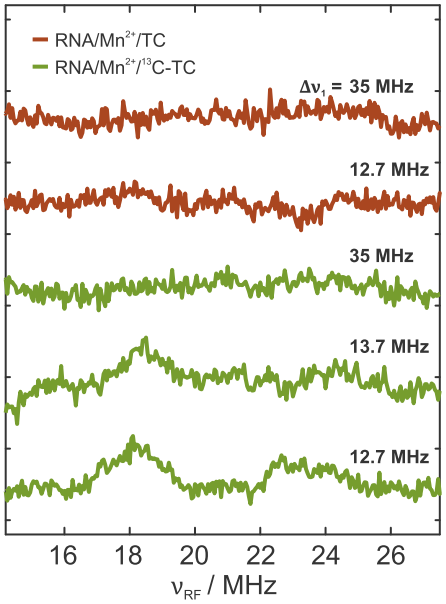

Fig. 7. Q-band THYCOS spectra of different Mn^{2+} complexes. Red: TC-aptamer with Mn^{2+} and TC, green: TC-aptamer with Mn^{2+} and ^{13}C-labeled TC. The RF pulse was used to sample the ^{31}P region, whereas the frequency offset $\Delta\nu_1$ of the ELDOR pulse was kept fixed at either 12.7 MHz, 13.7 MHz (^{13}C region) or 35.0 MHz (off-resonance). (For interpretation of the references to colour in this figure legend, the reader is referred to the web version of this article.)

THYCOS spectrum is therefore a superposition of two simultaneously excited THYCOS signals. As expected, the symmetry is lifted if the frequency offset of the ELDOR pulse is moved further away from the ^{13}C-Larmor frequency (*e.g.*, from 12.7 to 13.7 MHz, Fig. 7).

The asymmetric THYCOS spectrum recorded with $\Delta\nu_1 = 13.7$ MHz allows the determination of the sign of the ^{13}C-hyperfine coupling. As it is known that the isotropic hyperfine coupling of phosphorous is positive [42], the signal at 18.1 MHz must stem from the nuclear transition in the $|m_S = \alpha\rangle$ manifold. Positive heteronuclear THYCOS signals involve two nuclear transitions in different electron spin manifolds (Fig. 2C). The nuclear transition excited at $\Delta\nu_1 = 13.7$ MHz must therefore stem from the $|m_S = \beta\rangle$ manifold. If the nuclear transition in the $|\beta\rangle$ manifold appears at higher frequencies, the isotropic ^{13}C-hyperfine coupling must be positive (assuming $a_{iso} > T$), which is also in agreement with outer-electron transitions ENDOR studies and VMT Mims ENDOR experiments (Figs. S10 and S11).

If the ELDOR pulse is irradiated at $\Delta\nu_1$ values lower than 11.7 MHz, negative signals in the phosphorous region begin to appear (bold spectra in Fig. S20), which are reminiscent of signals due to off-resonance effects of the ELDOR pulse that where already reported by Litvinov et al. [42]. These signals start to build up around $\Delta\nu_1 \leqslant 10$ MHz, which perfectly agrees with the "cross-like" signals observed in the 2D EDNMR spectra (Fig. 5A and B). If ^{15}N-labeled RNA is used instead of nitrogen-unlabeled RNA, the negative THYCOS signals for a ^{15}N-labeled RNA are identical to the negative THYCOS signals for a nitrogen-unlabeled RNA (pale spectra in Fig. S20). This supports the idea that these signals are due to off-resonance effects and not due to ^{14}N-^{31}P correlation signals.

5. Conclusion

To the authors knowledge, this is the first time that 2D ELDOR-detected NMR and THYCOS are used to correlate ^{13}C and ^{31}P nuclei, located on two different molecules, to the same electron spin (Mn^{2+}).

2D-correlated hyperfine spectroscopy was able to show that TC binds to a TC-aptamer via a Mn^{2+} ion at physiological divalent metal ion concentrations of 1 mM. These results are in agreement with a study by Reuss et al. [11]. Although ITC experiments and fluorescence spectroscopy provide similar information by measuring thermodynamic parameters on a macroscopic scale, 2D EDNMR and THYCOS reveal complementary data on an atomistic level by directly investigating the nuclei and the electron spin incorporated in the center of the ternary complex.

Out of the two ^{31}P-hyperfine couplings, only the inner hyperfine coupling $A_{31P}(1)$ shows a clear correlation to ^{13}C-TC. Making statements about ^{13}C-^{31}P correlation signals involving the outer ^{31}P-hyperfine coupling based on 2D EDNMR and THYCOS data alone is difficult, as an insufficient resolution (2D EDNMR) or signal-to-noise ratio (THYCOS) would hamper the observation of such signals. The fact that ^{31}P-^{31}P THYCOS, however, shows clear self-correlation of the outer and the inner ^{31}P-hyperfine coupling but no correlation signals between the outer and inner ^{31}P-hyperfine coupling, underlines the hypothesis that both ^{31}P-hyperfine couplings must interact with different Mn^{2+} ions. In such a case, no ^{13}C-^{31}P correlation signals are expected that involve the outer ^{31}P-hyperfine coupling. This conclusion is in perfect agreement with the EDNMR-monitored freeze-thaw studies.

By using THYCOS, we were also able to determine the sign of the ^{13}C-hyperfine coupling of TC interacting with Mn^{2+}. Within the scope of this work, it is impossible to say how much of TC actually binds to the RNA. Monitoring the intensity of ^{13}C-^{31}P correlation signals in TC titration experiments should, however, give more insight into this question.

Although THYCOS and 2D EDNMR yield identical results, 2D EDNMR comes with the advantage of being far more sensitive. The total acquisition time of a complete 2D EDNMR spectrum was around 12 h, whereas the single 1D THYCOS spectrum recorded at $\Delta\nu_1 = 12.7$ MHz required an acquisition time of more than 24 h. The acquisition time for a complete 2D EDNMR spectrum for a less concentrated sample will be uneconomical long. However, if the nuclear species of interest is known, specific 2D EDNMR slices can be recorded, that contain the information of interest. The acquisition time for two 2D EDNMR slices (background slice and slice with nuclei of interest) was around 1 h. A shortcoming of 2D EDNMR is its reduced resolution in comparison to THYCOS, i.e., just as with 1D EDNMR signals, 2D EDNMR signals will not contain any information about the anisotropy of the hyperfine interaction. A good strategy is therefore to first perform a (complete) 2D EDNMR experiment and then record chosen THYCOS slices if the signal-to-noise ratio permits.

The implementation of non-linear frequency incrementation would help to increase the signal-to-noise ratio of 2D EDNMR data even further, as EDNMR spectra for a large part consist of baseline regions, that typically need less data points for a sufficient sampling than EDNMR signals. Such a feature is currently not implemented into Bruker spectrometers.

This study could demonstrate that THYCOS and in particular 2D EDNMR spectra or slices will be useful techniques to determine the binding of two biomolecules or small molecules/ligands to a paramagnetic transition metal, if no *prior* high-resolution knowledge about the system is available.

Acknowledgements

T.F.P. and B.S. acknowledge financial support from the Collaborative Research Center 902 – Molecular Principles of RNA-based regulation of the German Research Foundation (3214020004). A. M.B was supported by the Marie Curie GOIN program, and gratefully acknowledges her current fellowship support from the Royal Society and EPSRC for a Dorothy Hodgkin Fellowship (DH160004). We are grateful to Prof. Christiane Timmel and Dr. William Myers at the Centre of Advanced Electron Spin Resonance (CAESR), Oxford University for access to their facilities which are supported by the EPSRC (EPLO 11972/1) for some of the aforementioned experiments. We thank Dr. Björn Corzilius for useful comments on the manuscript.

Appendix A. Supplementary material

Supplementary data associated with this article can be found, in the online version, at https://doi.org/10.1016/j.jmr.2019.04.011.

References

[1] K.-M. Song, S. Lee, C. Ban, Aptamers and their biological applications, Sensors 12 (2012) 612–631, https://doi.org/10.3390/s120100612.
[2] C. Berens, A. Thain, R. Schroeder, A tetracycline-binding RNA aptamer, Bioorg. Med. Chem. 9 (2001) 2549–2556, https://doi.org/10.1016/S0968-0896(01)00063-3.
[3] H. Xiao, T.E. Edwards, A.R. Ferré-D'Amaré, Structural basis for specific, high-affinity tetracycline binding by an in vitro evolved aptamer and artificial riboswitch, Chem. Biol. 15 (2008) 1125–1137, https://doi.org/10.1016/j.chembiol.2008.09.004.
[4] M. Muller, J.E. Weigand, O. Weichenrieder, B. Suess, Thermodynamic characterization of an engineered tetracycline-binding riboswitch, Nucl. Acids Res. 34 (2006) 2607–2617, https://doi.org/10.1093/nar/gkl347.
[5] J.E. Weigand, B. Suess, Tetracycline aptamer-controlled regulation of pre-mRNA splicing in yeast, Nucl. Acids Res. 35 (2007) 4179–4185, https://doi.org/10.1093/nar/gkm425.
[6] P. Kötter, J.E. Weigand, B. Meyer, K.-D. Entian, B. Suess, A fast and efficient translational control system for conditional expression of yeast genes, Nucl. Acids Res. 37 (2009) e120.1–e120.7, https://doi.org/10.1093/nar/gkp578.
[7] M. Vogel, J.E. Weigand, B. Kluge, M. Grez, B. Suess, A small portable RNA device for the control of exon skipping in mammalian cells, Nucl. Acids Res. 46 (2018) e48.1–e48.12, https://doi.org/10.1093/nar/gky062.
[8] I. Chopra, M. Roberts, Tetracycline antibiotics: mode of action, applications, molecular biology, and epidemiology of bacterial resistance, Microbiol. Mol. Biol. Rev. 65 (2001) 232–260, https://doi.org/10.1128/MMBR.65.2.232-260.2001.
[9] D. Wunnicke, D. Strohbach, J.E. Weigand, B. Appel, E. Feresin, B. Suess, S. Muller, H.-J. Steinhoff, Ligand-induced conformational capture of a synthetic tetracycline riboswitch revealed by pulse EPR, RNA 17 (2011) 182–188, https://doi.org/10.1261/rna.2222811.
[10] U. Förster, J.E. Weigand, P. Trojanowski, B. Suess, J. Wachtveitl, Conformational dynamics of the tetracycline-binding aptamer, Nucl. Acids Res. 40 (2012) 1807–1817, https://doi.org/10.1093/nar/gkr835.
[11] A.J. Reuss, M. Vogel, J.E. Weigand, B. Suess, J. Wachtveitl, Tetracycline determines the conformation of its aptamer at physiological magnesium concentrations, Biophys. J. 107 (2014) 2962–2971, https://doi.org/10.1016/j.bpj.2014.11.001.
[12] T. Hetzke, M. Vogel, D.B. Gophane, J.E. Weigand, B. Suess, S.T. Sigurdsson, T.F. Prisner, Influence of Mg2+ on the conformational flexibility of a tetracycline aptamer, RNA 25 (2019) 158–167, https://doi.org/10.1261/rna.068684.118.
[13] J. De Vente, J. Zaagsma, The influence of the divalent cations Mn2+ and Mg2+ on the activation of particulate and digitonin-solubilized adenylate cyclase from rat fat cell membranes, Arch. Biochem. Biophys. 209 (1981) 249–255, https://doi.org/10.1016/0003-9861(81)90278-2.
[14] S.C. Dahm, O.C. Uhlenbeck, Role of divalent metal ions in the hammerhead RNA cleavage reaction, Biochemistry 30 (1991) 9464–9469, https://doi.org/10.1021/bi00103a011.
[15] T. Schweins, K. Scheffzek, R. Aßheuer, A. Wittinghofer, The role of the metal ion in the p21ras catalysed GTP-hydrolysis: Mn2+ versus Mg2+, J. Mol. Biol. 266 (1997) 847–856, https://doi.org/10.1006/jmbi.1996.0814.
[16] O. Schiemann, R. Carmieli, D. Goldfarb, W-band 31P-ENDOR on the high-affinity Mn2+ binding site in the minimal and tertiary stabilized hammerhead ribozymes, Appl. Magn. Reson. 31 (2007) 543–552, https://doi.org/10.1007/BF03166601.
[17] I. Kaminker, A. Sushenko, A. Potapov, S. Daube, B. Akabayov, I. Sagi, D. Goldfarb, Probing conformational variations at the ATPase site of the RNA helicase DbpA by high-field electron-nuclear double resonance spectroscopy, J. Am. Chem. Soc. 133 (2011) 15514–15523, https://doi.org/10.1021/ja204291d.
[18] J.A. Stull, T.A. Stich, R.J. Service, R.J. Debus, S.K. Mandal, W.H. Armstrong, R.D. Britt, 13C ENDOR reveals that the D1 polypeptide C-terminus is directly bound to Mn in the photosystem II oxygen evolving complex, J. Am. Chem. Soc. 132 (2010) 446–447, https://doi.org/10.1021/ja908688t.
[19] P.H. Oyala, T.A. Stich, J.A. Stull, F. Yu, V.L. Pecoraro, R.D. Britt, Pulse electron paramagnetic resonance studies of the interaction of methanol with the S2 state of the Mn4O5Ca cluster of photosystem II, Biochemistry 53 (2014) 7914–7928, https://doi.org/10.1021/bi501323h.
[20] T. Kumarevel, H. Mizuno, P.K.R. Kumar, Characterization of the metal ion binding site in the anti-terminator protein, HutP, of bacillus subtilis, Nucl. Acids Res. 33 (2005) 5494–5502, https://doi.org/10.1093/nar/gki868.

[21] K. Barth, S. Hank, P.E. Spindler, T.F. Prisner, R. Tampé, B. Joseph, Conformational coupling and trans-inhibition in the human antigen transporter ortholog TmrAB resolved with dipolar EPR spectroscopy, J. Am. Chem. Soc. 140 (2018) 4527–4533, https://doi.org/10.1021/jacs.7b12409.
[22] A. Albert, C.W. Rees, Avidity of the tetracyclines for the cations of metals, Nature 177 (1956) 433–434, https://doi.org/10.1038/177433a0.
[23] A. Yamaguchi, T. Udagawa, T. Sawai, Transport of divalent cations with tetracycline as mediated by the transposon Tn10-encoded tetracycline resistance protein, J. Biol. Chem. 265 (1990) 4809–4813, http://www.jbc.org/content/265/9/4809.long.
[24] S.R. Morrissey, T.E. Horton, C.V. Grant, C.G. Hoogstraten, R.D. Britt, V.J. DeRose, Mn2+-nitrogen interactions in RNA probed by electron spin-echo envelope modulation spectroscopy – application to the hammerhead ribozyme, J. Am. Chem. Soc. 121 (1999) 9215–9218, https://doi.org/10.1021/ja9921571.
[25] S.R. Morrissey, T.E. Horton, V.J. DeRose, Mn2+ sites in the hammerhead ribozyme investigated by EPR and continuous-wave Q-band ENDOR spectroscopies, J. Am. Chem. Soc. 122 (2000) 3473–3481, https://doi.org/10.1021/ja992989z.
[26] P. Manikandan, R. Carmieli, T. Shane, A.J. Kalb (Gilboa), D. Goldfarb, W-Band ENDOR investigation of the manganese-binding site of concanavalin A: determination of proton hyperfine couplings and their signs, J. Am. Chem. Soc. 122 (2000) 3488–3494, https://doi.org/10.1021/ja993395z.
[27] M. Bennati, M.M. Hertel, J. Fritscher, T.F. Prisner, N. Weiden, R. Hofweber, M. Spörner, G. Horn, H.R. Kalbitzer, High-frequency 94 GHz ENDOR characterization of the metal binding site in wild-type ras-GDP and its oncogenic mutant G12V in frozen solution, Biochemistry 45 (2006) 42–50, https://doi.org/10.1021/bi051156k.
[28] A.V. Astashkin, Y.E. Nesmelov, Mn2+ nucleotide coordination at the myosin active site as detected by pulsed electron paramagnetic resonance, J. Phys. Chem. B 116 (2012) 13655–13662, https://doi.org/10.1021/jp308423x.
[29] T.U. Nick, W. Lee, S. Koßmann, F. Neese, J. Stubbe, M. Bennati, Hydrogen bond network between amino acid radical intermediates on the proton-coupled electron transfer pathway of *E. coli* α2 ribonucleotide reductase, J. Am. Chem. Soc. 137 (2015) 289–298, https://doi.org/10.1021/ja510513z.
[30] P. Schosseler, T. Wacker, A. Schweiger, Pulsed ELDOR detected NMR, Chem. Phys. Lett. 224 (1994) 319–324, https://doi.org/10.1016/0009-2614, 94) 00548-6.
[31] L. Kulik, B. Epel, J. Messinger, W. Lubitz, Pulse EPR 55Mn-ENDOR and ELDOR-detected NMR of the S2-state of the oxygen evolving complex in photosystem II, Photosynth. Res. 84 (2005) 347–353, https://doi.org/10.1007/s11120-005-2438-7.
[32] M. Florent, I. Kaminker, V. Nagarajan, D. Goldfarb, Determination of the 14N quadrupole coupling constant of nitroxide spin probes by W-band ELDOR-detected NMR, J. Magn. Reson. 210 (2011) 192–199, https://doi.org/10.1016/j.jmr.2011.03.005.
[33] N. Cox, W. Lubitz, A. Savitsky, W-band ELDOR-detected NMR (EDNMR) spectroscopy as a versatile technique for the characterisation of transition metal-ligand interactions, Mol. Phys. 111 (2013) 2788–2808, https://doi.org/10.1080/00268976.2013.830783.
[34] E.M. Bruch, M.T. Warner, S. Thomine, L.C. Tabares, S. Un, Pulse electron double resonance detected multinuclear NMR spectra of distant and low sensitivity nuclei and its application to the structure of Mn(II) centers in organisms, J. Phys. Chem. B 119 (2015) 13515–13523, https://doi.org/10.1021/acs.jpcb.5b01624.
[35] N. Cox, A. Nalepa, W. Lubitz, A. Savitsky, ELDOR-detected NMR: a general and robust method for electron-nuclear hyperfine spectroscopy?, J Magn. Reson. 280 (2017) 63–78, https://doi.org/10.1016/j.jmr.2017.04.006.
[36] T. Hetzke, A.M. Bowen, T.F. Prisner, ELDOR-detected NMR at Q-band, Appl. Magn. Reson. 48 (2017) 1375–1397, https://doi.org/10.1007/s00723-017-0927-4.
[37] N. Wili, G. Jeschke, Chirp echo Fourier transform EPR-detected NMR, J. Magn. Reson. 289 (2018) 26–34, https://doi.org/10.1016/j.jmr.2018.02.001.
[38] A. Potapov, B. Epel, D. Goldfarb, A triple resonance hyperfine sublevel correlation experiment for assignment of electron-nuclear double resonance lines, J. Chem. Phys. 128 (2008) 052320.1–052320.10, https://doi.org/10.1063/1.2833584.
[39] I. Kaminker, T.D. Wilson, M.G. Savelieff, Y. Hovav, H. Zimmermann, Y. Lu, D. Goldfarb, Correlating nuclear frequencies by two-dimensional ELDOR-detected NMR spectroscopy, J. Magn. Reson. 240 (2014) 77–89, https://doi.org/10.1016/j.jmr.2013.12.016.
[40] M. Mehring, P. Höfer, A. Grupp, Pulsed electron nuclear double and triple resonance schemes, Berichte der Bunsengesellschaft für Phys. Chem. 91 (1987) 1132–1137, https://doi.org/10.1002/bbpc.19870911111.
[41] A. Potapov, I. Pecht, D. Goldfarb, Resolving ligand hyperfine couplings of type 1 and 2 Cu(II) in ascorbate oxidase by high field pulse EPR correlation spectroscopy, Phys. Chem. Chem. Phys. 12 (2010) 62–65, https://doi.org/10.1039/B919069D.
[42] A. Litvinov, A. Feintuch, S. Un, D. Goldfarb, Triple resonance EPR spectroscopy determines the Mn2+ coordination to ATP, J. Magn. Reson. 294 (2018) 143–152, https://doi.org/10.1016/j.jmr.2018.07.007.
[43] M. Ramirez Cohen, N. Mendelman, M. Radoul, T.D. Wilson, M.G. Savelieff, H. Zimmermann, I. Kaminker, A. Feintuch, Y. Lu, D. Goldfarb, Thiolate spin population of type I copper in azurin derived from 33S hyperfine coupling, Inorg. Chem. 56 (2017) 6163–6174, https://doi.org/10.1021/acs.inorgchem.7b00167.
[44] T. Wacker, G.A. Sierra, A. Schweiger, The concept of FID-detected hole-burning in pulsed EPR spectroscopy, Isr. J. Chem. 32 (1992) 305–322, https://doi.org/10.1002/ijch.199200038.
[45] B. Epel, D. Arieli, D. Baute, D. Goldfarb, Improving W-band pulsed ENDOR sensitivity – random acquisition and pulsed special TRIPLE, J. Magn. Reson. 164 (2003) 78–83, https://doi.org/10.1016/S1090-7807(03)00191-5.
[46] K. Keller, M. Zalibera, M. Qi, V. Koch, J. Wegner, H. Hintz, A. Godt, G. Jeschke, A. Savitsky, M. Yulikov, EPR characterization of Mn2+ complexes for distance determination with pulsed dipolar spectroscopy, Phys. Chem. Chem. Phys. 18 (2016) 25120–25135, https://doi.org/10.1039/C6CP04884F.
[47] S. Un, E.M. Bruch, How bonding in manganous phosphates affects their Mn(II)-31P hyperfine interactions, Inorg. Chem. 54 (2015) 10422–10428, https://doi.org/10.1021/acs.inorgchem.5b01864.
[48] S. Stoll, A. Schweiger, EasySpin, a comprehensive software package for spectral simulation and analysis in EPR, J. Magn. Reson. 178 (2006) 42–55, https://doi.org/10.1016/j.jmr.2005.08.013.
[49] B. Epel, P. Manikandan, P.M.H. Kroneck, D. Goldfarb, High-field ENDOR and the sign of the hyperfine coupling, Appl. Magn. Reson. 21 (2001) 287–297, https://doi.org/10.1007/BF03162408.
[50] M. Bennebroek, J. Schmidt, Pulsed ENDOR spectroscopy at large thermal spin polarizations and the absolute sign of the hyperfine interaction, J. Magn. Reson. 128 (1997) 199–206, https://doi.org/10.1006/jmre.1997.1234.